



HAL
open science

CFD Simulation for Characterization and Scale-Up of Pulsed Biomass Transport

Lucas Massaro Sousa, Benjamin Amblard, Sina Tebianian

► **To cite this version:**

Lucas Massaro Sousa, Benjamin Amblard, Sina Tebianian. CFD Simulation for Characterization and Scale-Up of Pulsed Biomass Transport. *Chemical Engineering Science*, 2022, 255, pp.117652. 10.1016/j.ces.2022.117652 . hal-03705435

HAL Id: hal-03705435

<https://ifp.hal.science/hal-03705435>

Submitted on 27 Jun 2022

HAL is a multi-disciplinary open access archive for the deposit and dissemination of scientific research documents, whether they are published or not. The documents may come from teaching and research institutions in France or abroad, or from public or private research centers.

L'archive ouverte pluridisciplinaire **HAL**, est destinée au dépôt et à la diffusion de documents scientifiques de niveau recherche, publiés ou non, émanant des établissements d'enseignement et de recherche français ou étrangers, des laboratoires publics ou privés.

1

2

3

CFD Simulation for Characterization and Scale-Up of Pulsed Biomass Transport

4

5

Lucas Massaro Sousa^{1,2}, Benjamin Amblard¹, Sina Tebianian^{1*}

6

7

8

¹Process Design and Modeling Division, IFP Energies Nouvelles, Rond-Point Échangeur de

9

Solaize, 69360 Solaize, France

10

²Wolfson Centre for Bulk Solids Handling Technology, Faculty of Engineering & Science,

11

University of Greenwich, Central Avenue, Chatham ME4 4TB, UK

* Corresponding author. E-mail addresses : sina.tebianian@ifpen.fr (S. Tebianian),
L.MassaroSousa@gre.ac.uk (L. Massaro Sousa)

12
13
14
15
16
17
18
19
20
21
22
23
24
25
26
27

ABSTRACT

Stable feeding of biomass powders into reactors represents a technical operational challenge for renewable energy generation. The injection of sawdust powders has been recently published with a horizontal pressurized gas injector under several experimental conditions. Valid numerical models are useful for hydrodynamic characterization of different equipment scales, such as computational fluid dynamics (CFD). In this study, the applicability of the CFD multiphase particle-in-cell approach (MP-PIC) for the considered injector is investigated. The model is tested under different operating conditions, showing relative deviations lower than 14% and 2% for solids flux and flow concentration experimental data. The effect of model inputs (mesh refinement, drag model, particle-to-wall interaction) on the system's hydrodynamics is discussed. The gas-solid flow hydrodynamics is obtained from the simulations providing additional insight on pulsed biomass transport. Ultimately, the model is used to investigate different injector diameters and to propose a feeder operation map as a function of dimensionless parameters.

Keywords: CFD, MP-PIC, Barracuda, pneumatic transport, bulk solids handling, non-mechanical feeder.

28 **1 Introduction**

29 Solid biomass wastes are generated in large amounts daily from industrial plants to
30 commercial businesses such as markets and restaurants, as well as from farm crops to residential
31 sector. Instances of common biomass residues are given by sawdust, spent coffee grounds,
32 sugarcane bagasse, rice husks, poultry litter and fruit peels. Decentralized generation of wastes
33 is an obstacle to its reuse because collection costs often outweigh reuse profits for such
34 inexpensive and difficult-to-handle bulk solids. On the other hand, wastes generation is
35 centralized in industries which allows for in-situ processing of biomass wastes into fuels or
36 renewable energy to improve companies' energy balance and reduce their carbon footprint
37 (McKendry, 2002; Perea-Moreno et al., 2019).

38 Fuels and renewable energy generation is directly related to efficient injection of biomass
39 particles into reactors producing a good penetration and mixing. This task is quite challenging
40 due to variations in samples' particle-size distribution, shape, and moisture content. Such
41 variations might worsen samples' flowability thus increasing its likelihood to clog feeders or
42 result in unstable flow (Ramírez-Gómez, 2016; Ilic et al., 2018). Biomass feeding to reactors
43 might be performed under batch, semi-continuous or continuous mode using mechanical or
44 non-mechanical feeding devices with associated pros and cons (Berruti et al., 2009; Dai and
45 Grace, 2011; Dai et al., 2012; Woodruff et al., 2012; Massaro Sousa and Ferreira, 2020b, 2020a;
46 Bai and Si, 2021; Gomes et al., 2021).

47 Recently, the hydrodynamics of a horizontal pressurized injector for feeding sawdust
48 powders (mean diameter from 447 to 1,130 μm) into fluidized beds has been experimentally
49 investigated with a high-speed camera (Massaro Sousa et al., 2021). The feeder showed stable
50 and wide range of operation, with solids mass flux ranging from 60 to 450 kg/m^2 representing
51 relevant conditions for solid pneumatic injection into fluidized beds. Given the available
52 experimental data, validation of numerical models based on computational fluid dynamics and

53 the development of scale-up rules is of great interest for advancing the state of the art for this
54 injector.

55 The commercial software CFPD Barracuda[®] implemented the multiphase particle-in-cell
56 approach (MP-PIC) to solve motion equations for gas/particles flow, and it is gaining interest
57 particularly because samples' particle-size distribution can be fully added and the simulations
58 are solved in a time-effective way. Equipment from bench-to-industrial scale have been already
59 simulated with this software for a wide range of applications, such as FCC regenerators,
60 fluidized beds under different regimes, coal gasifiers, chemical looping combustors, pneumatic
61 conveyors, etc (Chen et al., 2013; Amblard et al., 2015; Fotovat et al., 2015; Solnordal et al.,
62 2015; Ariyaratne et al., 2017; Chladek et al., 2018; Kraft et al., 2018; Tu and Wang, 2018;
63 Bandara et al., 2021; Pal and Theuerkauf, 2021; Sung et al., 2021).

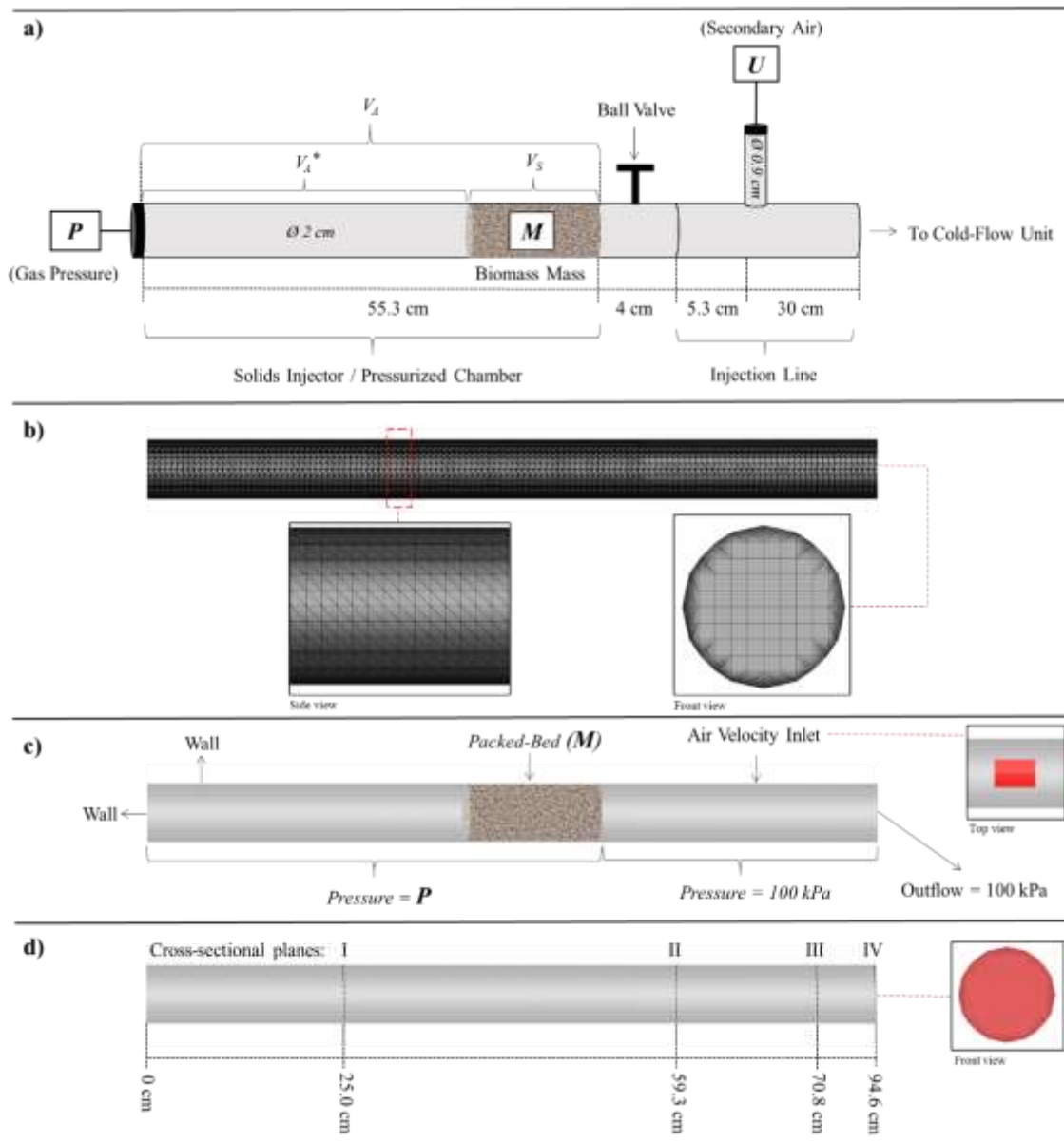
64 This paper presents the simulation of the mentioned pressurized gas injector with sawdust
65 powders using the CFD MP-PIC approach implemented in the Barracuda commercial code. To
66 the best of author's knowledge, this is the first simulative study addressing this type of non-
67 mechanical feeder, which deals with a fast release of pressurized gas to transport and inject
68 biomass powders into fluidized beds. First, the numerical model is compared with experimental
69 data and the effect of some model inputs on system's hydrodynamics is discussed. Finally, the
70 resulting model is used to extrapolate the feeder behavior at different operating and design
71 conditions.

72 **2 Material and Methods**

73 2.1 Experimental setup and data

74 The system dimensions described elsewhere (Massaro Sousa et al., 2021) are shown in
75 Fig. 1. It consists of a 0.02 m-internal diameter pipe that is divided in two sections (i.e.,
76 pressurized chamber and injection line) when the ball valve is closed. Initially, a given mass of

77 solids (M) is stored at the left section that is pressurized with different gas pressures (P). Once
 78 the ball valve is manually opened, the solids are transported to the cold-flow unit due to gas
 79 pressure release and momentum transfer. A continuous low secondary air velocity (U) can be
 80 also added to minimize the accumulation of powders in the injection line.



81
 82 **Fig. 1.** Injection system for sawdust powders: a) experimental unit, b) geometry and mesh, c) initial and
 83 boundary conditions, d) monitored planes: I, II, III, and IV.

84 The gas-solid hydrodynamics in the injection line has been investigated for different
 85 operating conditions of P and M , using a high-speed camera with acquisition rate of 3,000
 86 images/s (Massaro Sousa et al., 2021). The experimental flow time (t_e), mean solids mass flux
 87 (G_S) and solids flow concentration (ε_S) determined previously are used here for numerical

88 model testing. Note that t_e was measured experimentally and represents the time interval for
 89 powders to be released from the pressurized chamber and settle in the injection line. Another
 90 parameter considered in model/experiments comparison is R , which represents the mass of
 91 residual sawdust in the injection line after total gas release from the pressurized chamber
 92 divided by M .

93 Experimental data is shown in Table 1 for eight different injection conditions, with P and
 94 M range from 300 to 500 kPa and 0.003 to 0.024 kg, respectively. The secondary superficial
 95 gas velocity (U) was maintained at 4.4 m/s under all conditions. Note that V_S/V_A is the ratio of
 96 the initial volume of solids to the volume of the pressurized air at normal conditions in the
 97 chamber, as illustrated in Fig. 1a. This parameter impacts the solid concentration in the injection
 98 line:

$$\frac{V_S}{V_A} = \frac{M}{\left(V - \frac{M}{\rho_p}\right) \cdot \left(\frac{T_{ref}}{T}\right) \left(\frac{P}{P_{ref}}\right) \rho_p} \quad (1)$$

$$V_A = \frac{\left(V - \frac{M}{\rho_p}\right) \cdot \left(\frac{T_{ref}}{T}\right) \left(\frac{P}{P_{ref}}\right)}{V} \quad (2)$$

99 in which V is the volume of the pressurized chamber, equal to 1.73E-4 m³, whereas T_{ref} and P_{ref}
 100 are 273.15 K and 101.33 kPa, respectively.

101 **Table 1.** Summary of the injection conditions and experimental data.

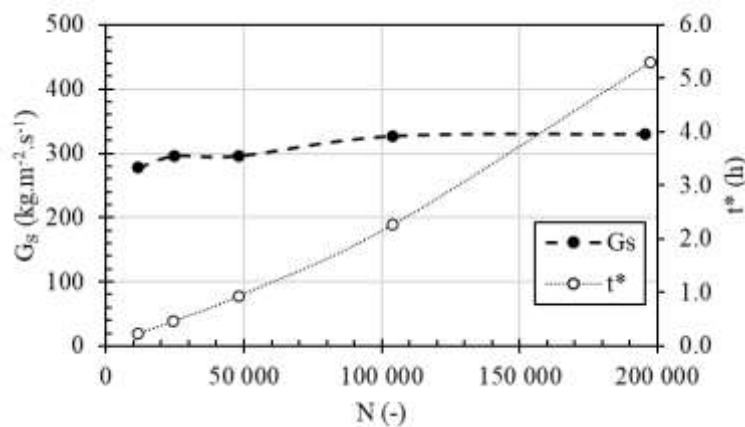
Tests	P (kPa)	M (kg)	V_S/V_A (-)	t_e (s)	G_S (kg·m ⁻² ·s ⁻¹)	ϵ_S (-)	R (%)
1	500	0.003	0.0036	0.045	210	0.058	0.3
2	400	0.003	0.0045	0.049	190	0.065	0.7
3	300	0.003	0.0060	0.096	100	0.089	3.1
4	300	0.006	0.0122	0.134	138	0.103	2.7
5	500	0.012	0.0152	0.134	284	0.113	0.9
6	400	0.012	0.0190	0.147	254	0.123	2.6
7	300	0.012	0.0253	0.167	216	0.137	5.6
8	500	0.024	0.0328	0.212	350	0.157	2.9

102 2.2 Injector geometry and mesh

103 The injector geometry was built in Catia V5[®] with the same dimensions of the
 104 experimental feeder. The mesh was generated directly on the simulation software, Barracuda

105 Virtual Reactor[®] 21.0, mainly with cubic cells except for a few that are cut by the walls, as
 106 shown in Fig. 1b. The ball valve and secondary air inlet are considered in the simulations
 107 through boundary conditions as given in Fig. 1c.

108 A mesh refinement study was conducted in one condition (Test 5) as presented in Fig. 2.
 109 The solids flux and simulation time (t^*) for different mesh refinement (N) are presented. While
 110 the simulation time increases up to 23 times from coarse to fine mesh, the solids flux shows a
 111 weak dependence with N , as G_S increases only about 15% in the same interval. Thus, to achieve
 112 a compromise between simulation time and accuracy, 48,100 cells was selected for simulating
 113 the 2-cm diameter solids injector. This compromise allows also to use similar cell sizes for the
 114 simulation of larger injector geometries as presented later in this paper. The selected mesh
 115 corresponds to a cell density of 162 cells/cm³ considering that the total geometry volume is
 116 2.97E-4 m³.



117 **Fig. 2.** Solids flux (G_S) and simulation time (t^*) as a function of number of cells (N). P and M are set as in test 5.
 118

119 2.3 Numerical model

120 The multiphase particle-in-cell (MP-PIC) method consists in using a hybrid
 121 Eulerian/Lagrangian approach to solve mass and momentum balances for gas and particles, as
 122 described below (Andrews and O'Rourke, 1996; Snider, 2001). The gas phase is treated as a
 123 continuum in a Eulerian framework by solving the averaged Navier-Stokes equations for mass
 124 and momentum:

$$\frac{\partial(\alpha_g \rho_g)}{\partial t} + \nabla \cdot (\alpha_g \rho_g \vec{u}_g) = 0 \quad (3)$$

$$\frac{\partial(\alpha_g \rho_g \vec{u}_g)}{\partial t} + \nabla \cdot (\alpha_g \rho_g \vec{u}_g \vec{u}_g) = -\alpha_g \nabla P + \alpha_g \rho_g \vec{g} + \nabla \tau_g - F \quad (4)$$

125 in which $\alpha_g, \rho_g, \vec{u}_g$ are the volume fraction, density, and velocity of the gas, respectively, while
 126 ∇P is the pressure gradient in the system. The gas stress tensor (τ_g) is shown in Eq. (5), while
 127 F represents the momentum exchange rate between gas and solid phase.

$$\tau_g = \mu_g (\nabla \vec{u}_g + \nabla^T \vec{u}_g) - \frac{2}{3} \mu_g \nabla \cdot \vec{u}_g I \quad (5)$$

128 Particles are treated with a hybrid Eulerian-Lagrangian approach where the mass and
 129 momentum balances for the solid phase are given by:

$$\frac{\partial(\alpha_s \rho_s)}{\partial t} + \nabla \cdot (\alpha_s \rho_s \vec{u}_s) = 0 \quad (6)$$

$$\begin{aligned} \frac{\partial(\alpha_s \rho_s \vec{u}_s)}{\partial t} + \nabla \cdot (\alpha_s \rho_s \vec{u}_s \vec{u}_s) + \nabla \tau_s + \alpha_s \nabla P = & \alpha_s \rho_s \vec{g} + \iint f m_p D(\vec{u}_g - \vec{u}_p) dm_p du_p \\ & - \nabla \left[\iint f m_p (\vec{u}_p - \vec{u}_s) (\vec{u}_p - \vec{u}_s) dm_p du_p \right] \end{aligned} \quad (7)$$

130 in which, the mean solid velocity (\vec{u}_s) and solid volume fraction (α_s) are defined by:

$$\vec{u}_s = \frac{1}{\alpha_s \rho_s} \iint f m_p \vec{u}_p dm_p du_p \quad (8)$$

$$\alpha_s = \iint f \frac{m_p}{\rho_s} dm_p du_p \quad (9)$$

$$\alpha_g + \alpha_s = 1 \quad (10)$$

131 In Eq. (7), f is the particle probability distribution (Snider, 2001) while D is the drag
 132 function. With the MP-PIC method, the particle probability distribution f is discretized into
 133 clouds which represent a certain number of particles with same diameter, mass, and velocity.
 134 At a given simulation time t , the cloud properties are interpolated to the Eulerian grid to solve
 135 the solid phase equations. Once the equations are solved on the grid, the Eulerian grid properties
 136 such as gas velocities, gas pressure gradients and solids stress gradients are interpolated back

137 to the clouds to update their positions and velocity using a lagrangian approach with the
 138 following equations. The position of the cloud at the next time step x_p^{n+1} is calculated with Eq.
 139 (11) where x_p^n is the cloud position at the current time step, Δt is the time step and U_p^{n+1} is the
 140 cloud velocity at the next time step.

$$x_p^{n+1} = x_p^n + \Delta t U_p^{n+1} \quad (11)$$

141 Then, U_p^{n+1} is calculated as:

$$U_p^{n+1} = \frac{U_p^n + \Delta t \left[D U_{g,p}^{n+1} - \frac{1}{\rho_s} \nabla P_p^{n+1} + g - \frac{1}{\alpha_s \rho_s} \nabla \tau_p^{n+1} \right]}{1 + \Delta t D} \quad (12)$$

142 In which $U_{g,p}^{n+1}$ is the gas velocity at $t+\Delta t$ interpolated to the cloud position; P_p^{n+1} is the pressure
 143 at $t+\Delta t$ interpolated to the cloud position; τ_p^{n+1} is the solid stress at $t+\Delta t$ interpolated to the cloud
 144 position.

145 One of the drag models employed in this study is based on Energy-Minimization Multi-
 146 Scale (EMMS) approach, with the following expression:

$$D = \frac{9}{8} \frac{\mu_g}{\rho_p d_p^2} f_e \quad (13)$$

$$f_e = \begin{cases} \frac{1}{18\alpha_g} \left(c_0 \frac{\alpha_s}{\alpha_g} + c_1 Re \right) & \alpha_g < 0.74 \\ (c_2 + c_3 Re^{c_{15}}) \omega & \alpha_g \geq 0.74 \text{ and } Re < 1000 \\ c_4 \frac{Re}{24} \omega & \alpha_g \geq 0.74 \text{ and } Re > 1000 \end{cases} \quad (14)$$

$$\omega = \begin{cases} c_5 + \frac{c_6}{4(\alpha_g + c_7)^2 + c_8} & 0.74 \leq \alpha_g \leq 0.82 \\ c_9 + \frac{c_{10}}{4(\alpha_g + c_{11})^2 + c_{12}} & 0.82 < \alpha_g \leq 0.97 \\ c_{13} + c_{14} \alpha_g & 0.97 < \alpha_g \leq 1 \end{cases} \quad (15)$$

147 in which, $c_0=150$, $c_1=1.75$, $c_2=1.0$, $c_3=0.15$, $c_4=0.44$, $c_5=-0.576$, $c_6=0.0214$, $c_7=-0.7463$,
 148 $c_8=0.0044$, $c_9=-0.0101$, $c_{10}=0.0038$, $c_{11}=-0.7789$, $c_{12}=0.0040$, $c_{13}=-31.8295$, $c_{14}=32.8295$, and
 149 $c_{15}=0.687$. Note that the EMMS is already implemented in Barracuda and the values for the
 150 constants are based on a previous study (Yang et al., 2004).

151 The solid phase stress tensor (τ_s), also present in Eq. (7), is given by:

$$\tau_s = \frac{10P_s\alpha_s^\beta}{\max[\alpha_{s,max} - \alpha_s, \varepsilon_p(1 - \alpha_s)]} \quad (16)$$

152 in which P_s is a constant with units of pressure (1 Pa), $\alpha_{s,max}$ is the solid volume fraction at
153 close pack, β is a constant between 2 and 5 and a value of 3 was utilized in this study, and ε_p
154 is a very small number (10^{-8}). Comparatively, the modeling of the solid phase stress tensor is
155 simpler than the one used in the kinetic theory of granular flow where a specific equation is
156 used for the transport of the granular temperature (Lun et al., 1984; Gidaspow, 1994).

157 The collisions of the solid phase with walls are considered with Eq. (17). The resulting
158 particles cloud velocity (\vec{u}_p) following a wall impact, at the instant $n+1$, is decreased by normal
159 (η_n) and tangential (η_t) retention parameters for momentum losses and angle of impact with
160 respect to the vertical direction (θ):

$$\vec{u}_p^{n+1} = [(\eta_n - \eta_t)(1 - \cos \theta) + \eta_n] \vec{u}_p^n \quad (17)$$

161 2.4 Simulation conditions

162 The solid injection simulations were performed under the conditions shown in Table 1.
163 Simulations were performed in Barracuda Virtual Reactor[®] 21.0 with a Linux computer (Intel[®]
164 Xeon[®], E5-1620 v3, 3.5 GHz) during a total simulation time of 0.3s, and with a time step of
165 10^{-5} s. Simulating 0.3s is sufficient to cover all experimental conditions because the maximum
166 experimental flow time is 0.212s (test 8).

167 The initial and boundary conditions are depicted in Fig. 1c. A given mass of sawdust
168 powders (M) is initially packed in the solids injector, at the same location as experimentally,
169 while the gas phase is pressurized at a given P in the chamber region. The pressure on the
170 injection line and ball valve regions are set as 100 kPa (atmospheric pressure), and outflow for
171 gas and solids is set at the boundary of the cold-flow unit also with 100 kPa. A secondary air
172 velocity (U) of 4.4 m/s is added perpendicularly to the injection line through a square plane of

173 equal area than the experimental inlet. Finally, a wall boundary condition is set on the left end
 174 of the pressurized chamber.

175 Some planes were created in the geometry to monitor the gas-solid flow, as shown in Fig.
 176 1d, such as planes I, II, III, and IV. Flow data was acquired every 10^{-4} s to fully capture the gas-
 177 solid hydrodynamics in the injection line, which physically corresponds to a fast transport of
 178 bulk solids by pressurized gas release. Note that the region between planes II and III
 179 corresponds to the same location that the gas-solid flow was assessed experimentally with the
 180 high-speed camera (Massaro Sousa et al., 2021).

181 In the simulations, mean values for G_S and ε_S were obtained considering the positions and
 182 experimental data acquisition methods (Massaro Sousa et al., 2021). Thus, the solids mass flux
 183 passing through plane III was monitored and integrated until 99.5% of the cumulative mass
 184 curve is reached ($M_{99.5\%}$). The corresponding flow time $t_{99.5\%}$ provides the G_S as:

$$G_S = \left(\frac{M_{99.5\%}}{A \cdot t_{99.5\%}} \right) \quad (18)$$

185 in which A is the cross-sectional area of the injection line of $3.14E-4 \text{ m}^2$. The mean solids
 186 fraction is obtained iteratively by Eq. (19), which is the same equation used to average the
 187 experimental results. Note that ε_S calculated from Eq. (19) is a volumetric ratio which agrees
 188 with the solids fraction definition:

$$\varepsilon_S = \frac{Q_S}{Q_t + Q_S} = \frac{\frac{G_S A}{\rho_p \varepsilon_S}}{Q_t + \frac{G_S A}{\rho_p \varepsilon_S}} \quad (19)$$

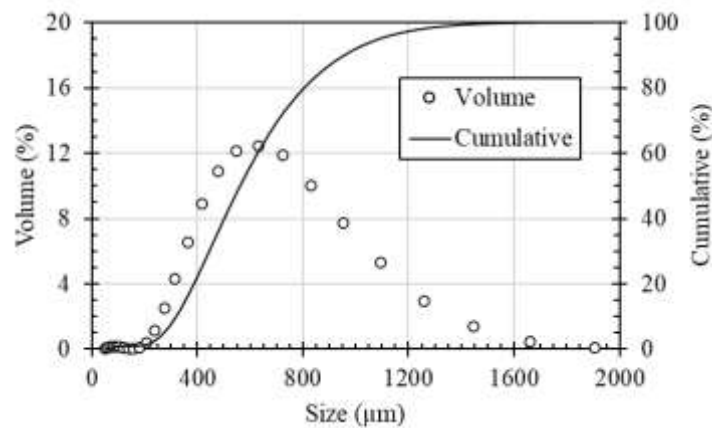
189 in which Q_t is the volumetric gas flowrate in plane III averaged until $t_{99.5\%}$. We have also
 190 verified that using Eq. (19) is consistent with the cross-sectional mass-weighted average ε_S
 191 gathered from the simulations. Finally, R is calculated by dividing the mass of solids
 192 accumulated in the injection line at the end of simulation by M .

193 The drag model used was based on the Energy-Minimization Multi-Scale (EMMS), and
 194 the normal (η_n) and tangent-to-wall (η_t) parameters were set as 0.70. A detailed study about

195 these parameters is presented in Sections 3.1 and 3.2, respectively. Other variables have been
196 maintained as Barracuda's default, such as: close pack volume fraction of 0.60, diffuse bounce
197 of 5, and particle-particle interactions ($P_s=1$ Pa, $\beta=3$, $\varepsilon_p=10^{-8}$, $m=40\%$).

198 2.5 Sawdust properties

199 The particle size distribution of the sawdust sample is shown in Fig. 3 with d_{50} of 647
200 μm . The cumulative curve has been fully inserted in the simulations along with the particle
201 density of $1,030$ kg/m^3 (Geldart B), and initial particle volume fraction of 0.21 (averaged
202 between loose and tapped conditions). Note that the particle volume fraction of sawdust is
203 within the range of typical values for other biomass particles, generally from 0.07 to 0.30, as
204 reported in the literature (Tannous et al., 2013; Dhiman et al., 2016; Massaro Sousa and
205 Ferreira, 2019). The methods for sample characterization are presented in detail elsewhere
206 (Massaro Sousa et al., 2021). The particle shape factor was considered as 1 in the simulations.



207
208 **Fig. 3.** Particle size distribution for the sawdust sample with d_{10} , d_{50} , and d_{90} equal to 370, 647, and 1,100 μm .

209 3 Results and Discussion

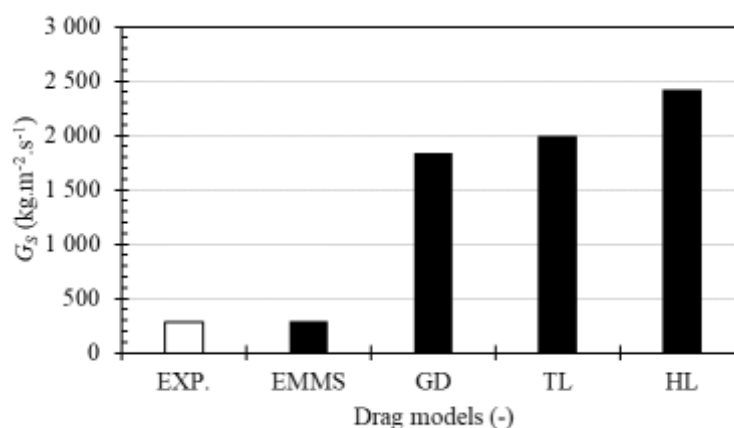
210 3.1 Effect of the drag model

211 In the following sections, the influence of the drag model and particle-to-wall interactions
212 are investigated to find the best set that represents the experiments. To minimize the number of

213 simulations, the parameters' effect were studied under operational settings of test 5 (Table 2),
214 however similar effects are expected under conditons of tests 1-8.

215 Different drag models have been evaluated to predict the horizontal transport of sawdust
216 from the injector, consisting of Gidaspow (GD), Turton-Levenspiel (TL), Haider-Levenspiel
217 (HL), and Energy-Minimization Multi-Scale (EMMS). These drag models are already
218 implemented in Barracuda Virtual Reactor[®] 21.0 and commonly used for gas-solid flows
219 (Turton and Levenspiel, 1986; Haider and Levenspiel, 1989; Gidaspow, 1994; Yang et al.,
220 2004; Chen et al., 2013).

221 In Fig. 4, simulation results for solids mass flux matches experimental data (white bar)
222 accurately with the EMMS drag model, whereas the other homogeneous drag models
223 overestimated the solids flux by 6 to 9 times. Thus, the EMMS has been selected for the
224 simulations of this work. Previous MP-PIC studies have also demonstrated improved
225 hydrodynamics predictions with the EMMS method, while overstimulation of fluidization
226 patterns were observed with the other drag models for circulating fluidized beds with Geldart
227 B and D (Kraft et al., 2017; Kraft et al., 2018; Tu and Wang, 2018) and fluidized beds with
228 Geldart A (Feng et al., 2018). A recent MP-PIC study on pneumatic conveying of drill cuttings
229 ($d_{50}=290 \mu\text{m}$, $\rho_p=2,715 \text{ kg/m}^3$, Geldart B) used the Gidaspow drag model multiplied by 0.50 to
230 reduce the drag force and match the pressure drop and particle velocity in their pipeline (Sung
231 et al., 2021).



232

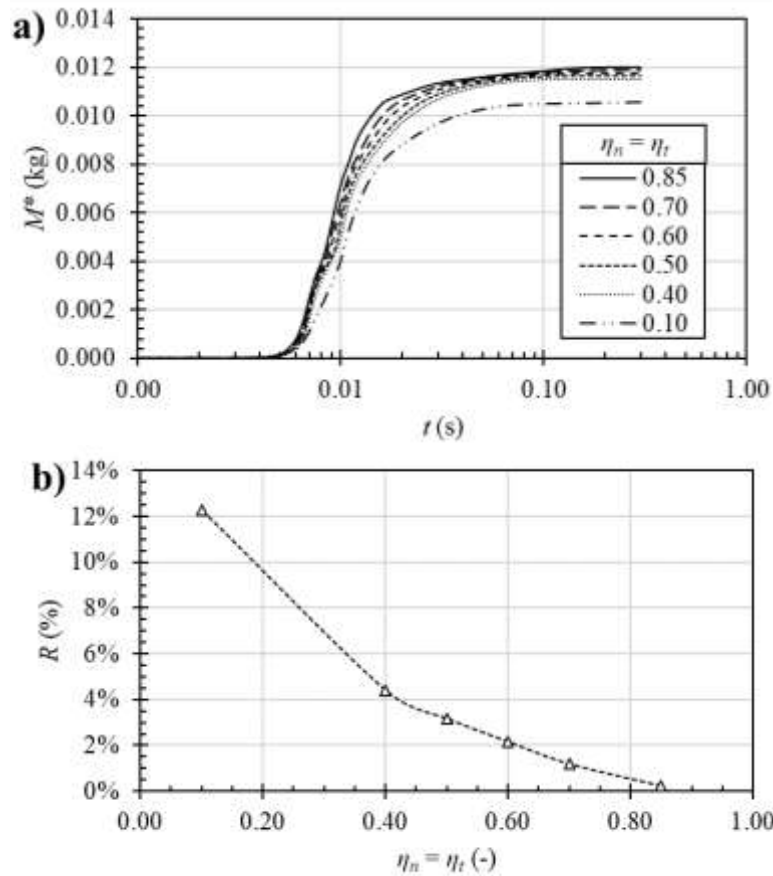
233 **Fig. 4.** Solids flux (G_S) for various drag models with P and M set as in test 5.

234 3.2 Effect of particle-to-wall collision

235 Particle-to-wall interactions are addressed in Barracuda[®] with two main parameters,
236 accounting for normal (η_n) and tangent (η_t) collisions with the wall. A value of 1.0 indicates a
237 perfectly elastic collision, which means that the particle bounce back from or slide tangent to
238 the wall with the same momentum before the contact, whereas 0.0 indicates that the momentum
239 is entirely dissipated. Information about such parameters are difficult to be obtained
240 experimentally, thus different values have been numerically investigated from 0.85 to 0.10, and
241 its effect on the injector dynamics are presented in Fig. 5. Since both parameters are unknown,
242 we used the same values for η_n and η_t while analysing their effect on the responses.

243 The cumulative mass of sawdust passing through plane III (M^*) is shown in Fig. 5a during
244 0.3s of simulation for different η_n and η_t . The shape of the curves are similar among each other,
245 with an initial fast transport of solids followed by an asymptotical pattern due to the decrease
246 of the pressurized chamber gas, which is the driving force for the transport of solids. Besides,
247 curves become less inclined as parameters values decreases to 0.10, indicating that the mean
248 solids mass flux decreases by decreasing η_n and η_t . For example, G_S decrease by 11% from 0.85
249 to 0.10. Moreover, as shown in Fig. 5b, there is a significant increase in the accumulation of
250 sawdust in the injection line (R), from 0.2 to 12.3%, by decreasing η_n and η_t from 0.85 to 0.10
251 which is due to higher friction among the particles and wall.

252 These results are in agreement with the expected behavior, since enhanced loss of
253 momentum occurs with lower parameters values, hence decreasing G_S and increasing R . For
254 the simulation of the solids injector with sawdust, η_n and η_t have been fixed at 0.70 to match
255 experimental data for test 5 (R and G_S). Note that 0.70 is within the range of recommended
256 values in Barracuda's manual, as typical parameters values of 0.50 and 0.85 are used for soft
257 and hard particles, respectively.



258

259

260

261

Fig. 5. Simulated results for different η_n and η_t : a) sawdust mass passing through plane III (M^*), and b) accumulation of powders in the injection line (R). P and M are set as in test 5.

262 3.3 Numerical model testing

263

264

265

266

267

268

In this section, the numerical model is tested under different operating conditions, tests 1 to 8 (Table 1). A consistent quantitative agreement between simulated and experimental data is presented in Fig. 6, in terms of solids mass flux, flow time, and flow concentration. On average, relative deviations were lower than 14, 11, and 2% for G_S , ε , and t_e , respectively, from tests 1 to 8 ($0.0036 \leq V_S/V_A \leq 0.0328$). The relative deviations were calculated as the difference between simulated and experimental values divided by the experimental one.

269

270

271

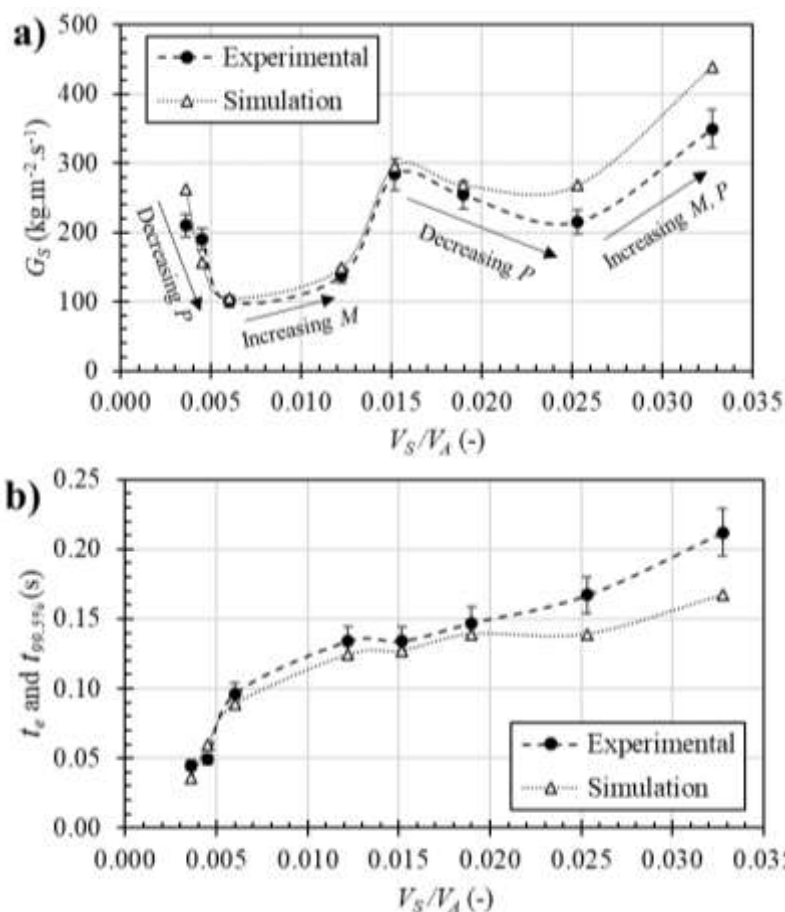
272

273

As demonstrated experimentally (Massaro Sousa et al., 2021), depending on the initial settings for M and P , different solids mass flux and flow concentrations can be obtained in the injection line. The numerical model accurately reproduced such behaviors from tests 1-8. Under stable operating conditions, higher solids mass fluxes are obtained by using higher gas pressure and/or initial mass of solids in the injector.

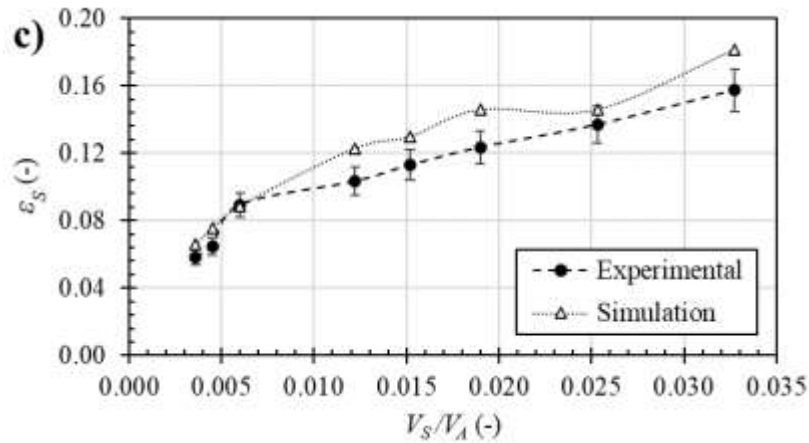
274 Fig. 6a presents the trends of simulation data under decreasing P (points 1 to 3, and 5 to
 275 7) or increasing M (points 3 to 4, and 7 to 8) for different V_S/V_A values. The qualitative
 276 experimental behavior was reproduced extremely well by the simulations, specially for
 277 $0.005 \leq V_S/V_A \leq 0.020$ with relative deviations of 5% (within the experimental error bars). Outside
 278 of this range, the deviations reached up to 20%, possibly because the pulse injections were
 279 either more dilute or dense compared to the conditions of test 5 ($V_S/V_A=0.0152$), which was
 280 used for selecting the drag model and particle-wall parameters.

281 Moreover, it was observed experimentally that both flow time and solids concentration
 282 in the injection line increase as V_S/V_A increases (i.e., with increasing initial solids ratio in the
 283 injector), and the numerical model also predicts it as presented in Figs. 6b and 6c.



284

285

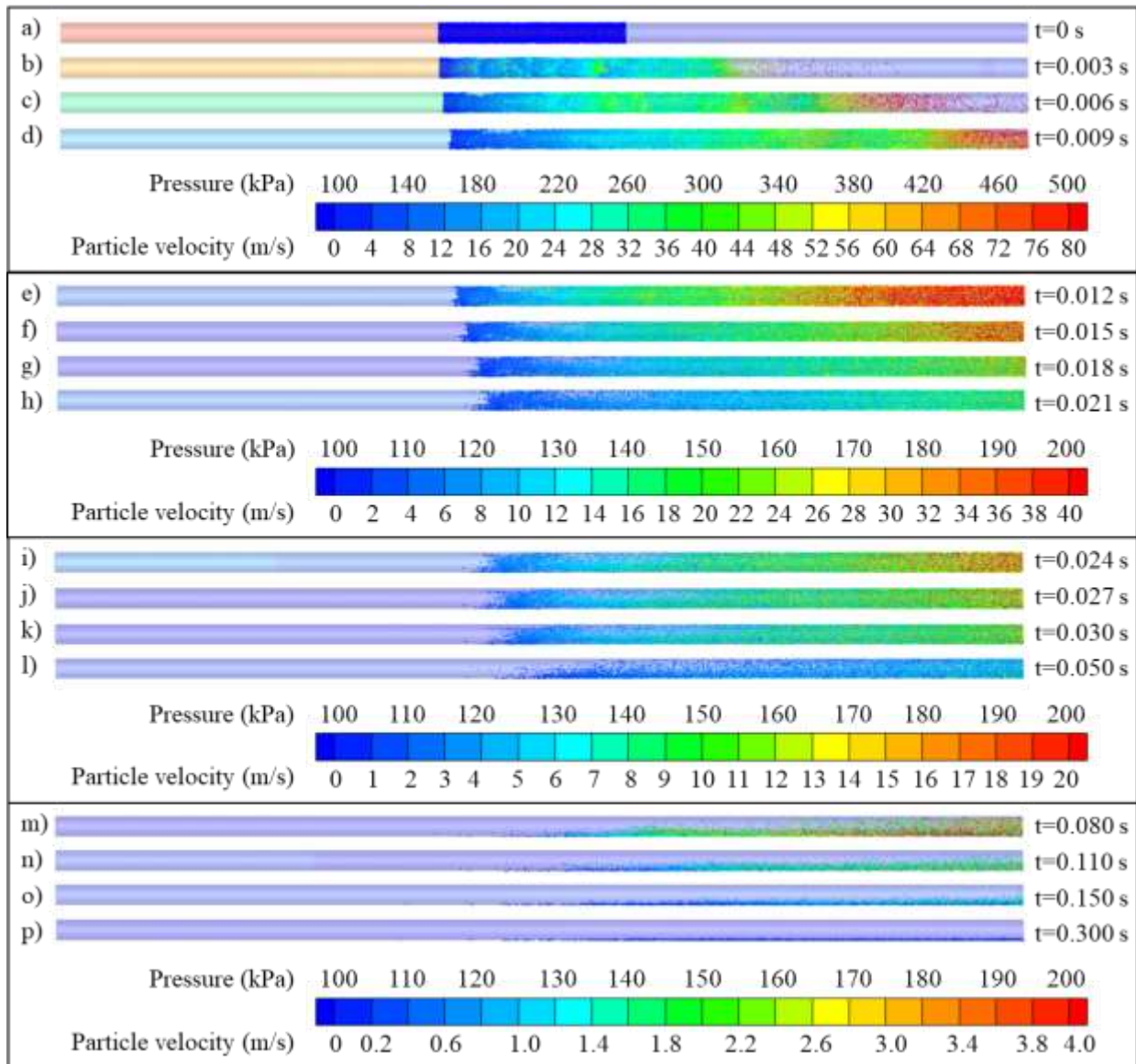


286
287 **Fig. 6.** Experimental and simulated data for a) G_S , b) t_e and $t_{99.5\%}$, and c) ϵ_S .

288 3.4 Contours for solid and gas phases

289 The transient behavior for the injection of sawdust powders is illustrated in Fig. 7 under
290 test 5 conditions. The discrete phase is coloured according to the particle velocity, from 0 to 80
291 m/s, while the continuous phase is painted in terms of gas pressure, from 100 to 500 kPa, as it
292 is the driving force for the solids transport. At $t=0$ s, the particles are at rest and the gas is
293 pressurized in the chamber with $P=500$ kPa.

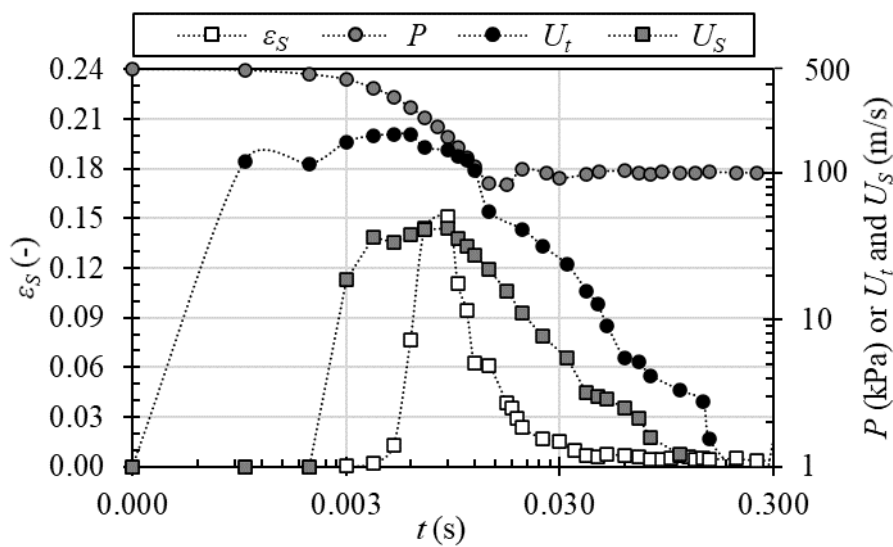
294 As soon as the simulation starts, the gas is released downstream with P dropping rapidly
295 to 400, 300, and 200 kPa in 0.009s, as shown in Figs. 7b to 7d, respectively. In this interval, the
296 solids are accelerated by transfer of gas momentum, and there is a distribution of particle
297 velocities and concentrations along the geometry. At the injection line section, there is initially
298 a dilute transport of solids at high-speed (Fig. 7b), followed by a more dense flow with velocity
299 from 30 to 80 m/s (Figs. 7c to 7d). On the other hand, at the pressurized chamber region the
300 solids velocity are generally lower than 30 m/s. These features are in line with experimental
301 observations with a high-speed camera at 3,000 frames per second (Massaro Sousa et al., 2021).



302 **Fig. 7.** Countours for particles velocity (discrete phase colour) and gas pressure (background colour) at different
 303 times. P and M are set as in test 5.
 304

305 In the images, the coloring scale range has been reduced to better assess the phenomena.
 306 From Fig. 7e and onwards, a decelerating flow of solids is verified due to a combined effect of
 307 pressurized gas emptying at the solids injector chamber ($P \approx 100$ kPa) and loss of momentum by
 308 particle-particle and particle-wall collision. The solids are homogeneously distributed along
 309 injection's line diameter, until they begin to settle at the lower section of the tube (Fig. 7m),
 310 and their residual movement is due to the powder's inertia and bouncing. Finally, there is almost
 311 no transport of powders at $t=0.3s$, and the residual solids accumulate throughout the base of the
 312 injection line (Fig. 7p).

313 The transient behavior can be also visualized in Fig. 8, in which the flow concentration
 314 (ε_S) and total interstitial gas velocity (U_t) were averaged in the cross-sectional plane III over
 315 time, while the gas pressure was averaged in plane I (Fig. 1d). As previously described, there
 316 is a fast decrease in P due to gas release with ball valve opening, resulting in the transport of
 317 solids with peak values for ε_S up to 0.16, for total gas velocity up to 200 m/s, and for mean
 318 cross-sectional solids velocity up to 45 m/s. As P reaches atmospheric conditions, there is a
 319 deceleration pattern for ε_S , U_t and U_S until the remaining solids settle at the injection line.



320 **Fig. 8.** Flow concentration (ε_S) total interstitial gas velocity (U_t), cross-sectional solids velocity (U_S) and pressure
 321 (P) over time for conditions of test 5.
 322

323 3.5 Model extrapolation: feeder operation map

324 It is interesting to investigate model's responses outside of the interval that has been tested
 325 against experimental data, particularly for operating conditions that are difficult or dangerous
 326 to be implemented experimentally. Therefore, higher gas pressures are analyzed here up to
 327 1,650 kPa, which represents a 3.3-fold increase compared to the maximum one used in the
 328 experiments ($P=500$ kPa) (Massaro Sousa et al., 2021). The injector dimensions were
 329 maintained as shown in Fig. 1a, which means that, at maximum, 0.0364 kg of sawdust can be
 330 inserted into the pressurized chamber region.

331 The simulations were performed under three solids loading conditions, V_S/V_A of 0.015,
332 0.025, and 0.035. The solids mass flux is shown in Fig. 9a as a function of the gas pressure. The
333 trend of the curves are similar, with an initial linear increase of G_S as P increases, until it reaches
334 a maximum value, followed by a decreasing trend for G_S . For example, with the solids loading
335 of 0.015, G_S can be adjusted from 100 to 650 kg/m²s by increasing P up to 1,650 kPa.

336 In Fig. 9b, G_S is plotted as a function of V_A that is a dimensionless parameter related to
337 the amount of pressurized air representing the driving force for the solids transport with this
338 injector. The curves behavior are similar to the ones described in Fig. 9a, however with the
339 advantage that the dimensionless parameters (V_A and V_S/V_A) are dissociated from specific
340 experimental conditions resulting in a more general description of the phenomena. Note that
341 these parameters can be easily calculated before any injection of solids (i.e., from initial P and
342 M conditions) with Eqs (1) and (2).

343 To explain the maximum of G_S in the curves, three points have been highlighted in Fig.
344 9b and are illustrated in Fig. 9d. These points are under the same V_S/V_A ratio with increasing
345 V_A , hence more solids are present in the pressurized chamber from points (1) to (3). As also,
346 observed experimentally, a large amount of solids in the pressurized chamber provides a
347 significant length that requires higher amount of gas for solids transport compared to when a
348 smaller portion of the chamber is occupied. However, as shown in Fig. 9d, this additional gas
349 is limited because the pressurized chamber length is fixed, then there is a decrease in G_S as the
350 chamber approaches its maximum powder filling limit.

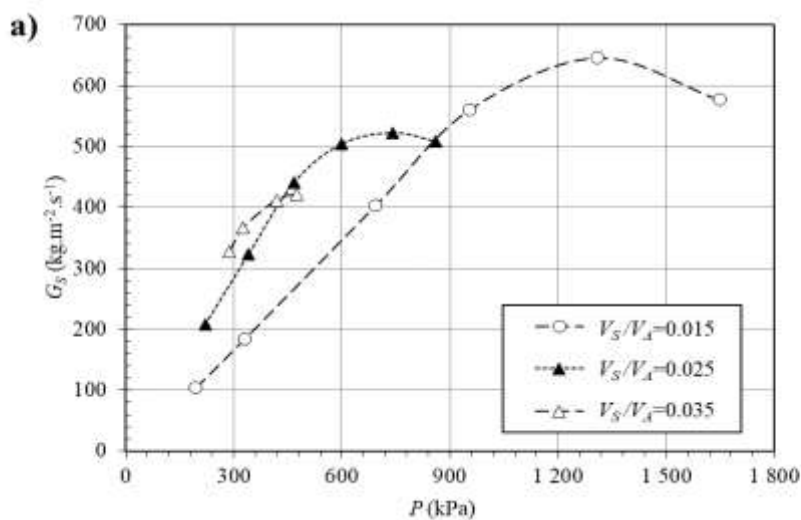
351 The phenomena described in the previous paragraph, results that, if there is not a
352 significant amount of pressurized gas available on the left side of the packed bed (in the
353 pressurized chamber) to push the powders ensemble, then the feeders performance is
354 jeopardized, which means that there is a decrease in G_S and significative accumulation of solids
355 in the injection line (e.g., $R>10\%$) (Massaro Sousa et al., 2021). There is a dimensionless

356 parameter, V_A^* , that captures the portion of air pressurized on the left side of the packed bed, as
 357 illustrated in Fig. 9d. It is calculated by considering the mean bulk density between loose and
 358 tapped conditions (ρ_m of 215 kg/m³):

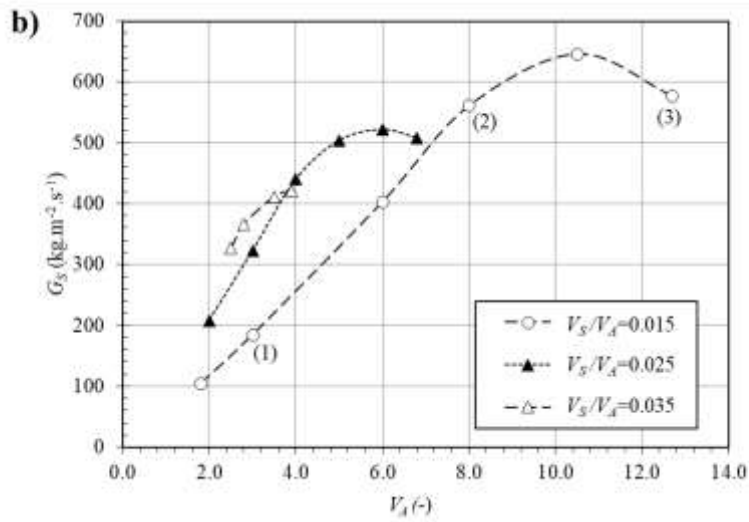
$$V_A^* = \frac{\left(V - \frac{M}{\rho_m}\right) \cdot \left(\frac{T_{ref}}{T}\right) \left(\frac{P}{P_{ref}}\right)}{V} \quad (20)$$

359 Experimentally the feeder malfunction occurred for $V_A^* \leq 1.4$, thus the simulations were
 360 performed here considering $V_A^* = 1.6$ as the operating limit. The G_S curve plotted as a function
 361 of V_A^* is presented in Fig. 9c for the studied V_S/V_A , showing the curve inversion pattern
 362 (maximum G_S point) as a consequence of increasing solids loading in the injector.

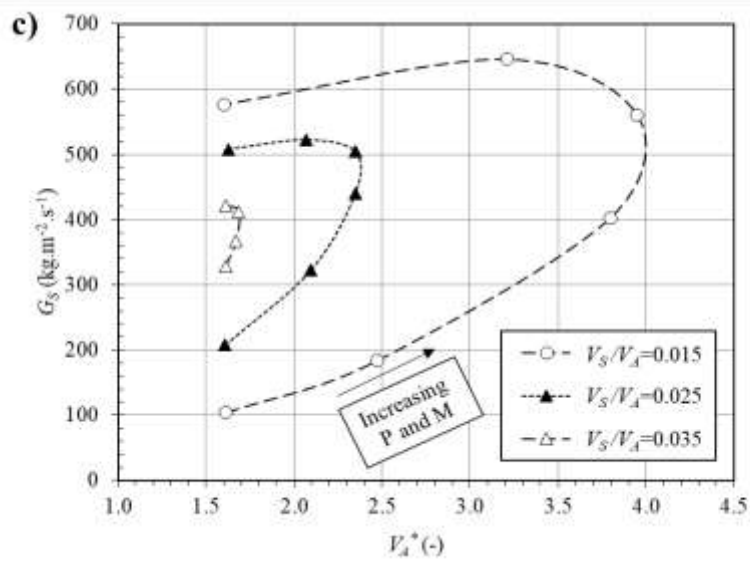
363 Another remark on the operation map (Fig. 9c) is that for a given V_A , the higher the initial
 364 solids inventory (V_S/V_A) the higher G_S because the injection of sawdust occurs in a more dense
 365 condition as was the case experimentally. This is highlighted in Fig. 9e by the mean flow
 366 concentration from 0.12 to 0.20, in the interval of $0.015 \leq V_S/V_A \leq 0.035$. Ultimately, Figs. 9b and
 367 9e are useful for estimating G_S and ε_S for the actual injector by interpolating the curves, which
 368 are valid for a broad range of conditions (i.e., $0.015 \leq V_S/V_A \leq 0.035$, and $1.8 \leq V_A \leq 12.7$, with the
 369 restrictive condition that $V_A^* \geq 1.6$), at least according to the simulations.



370

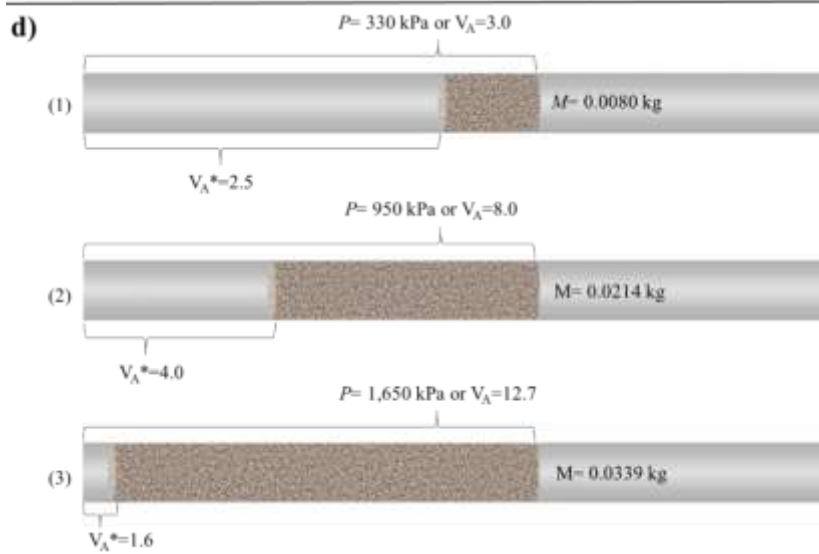


371

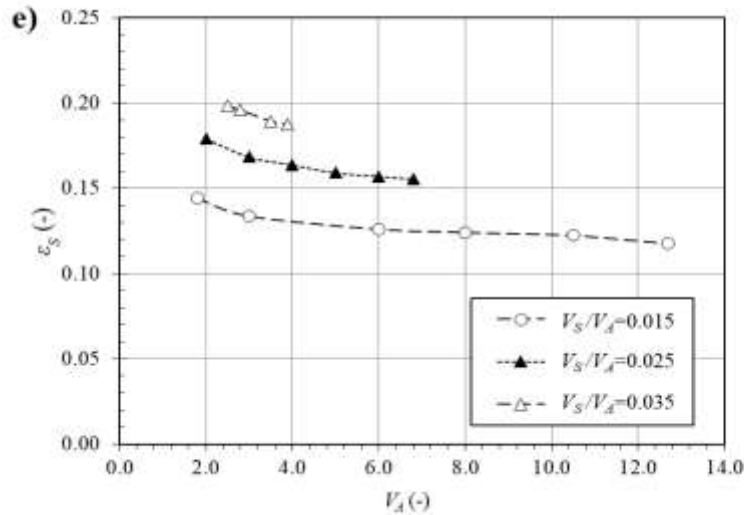


372

373



374



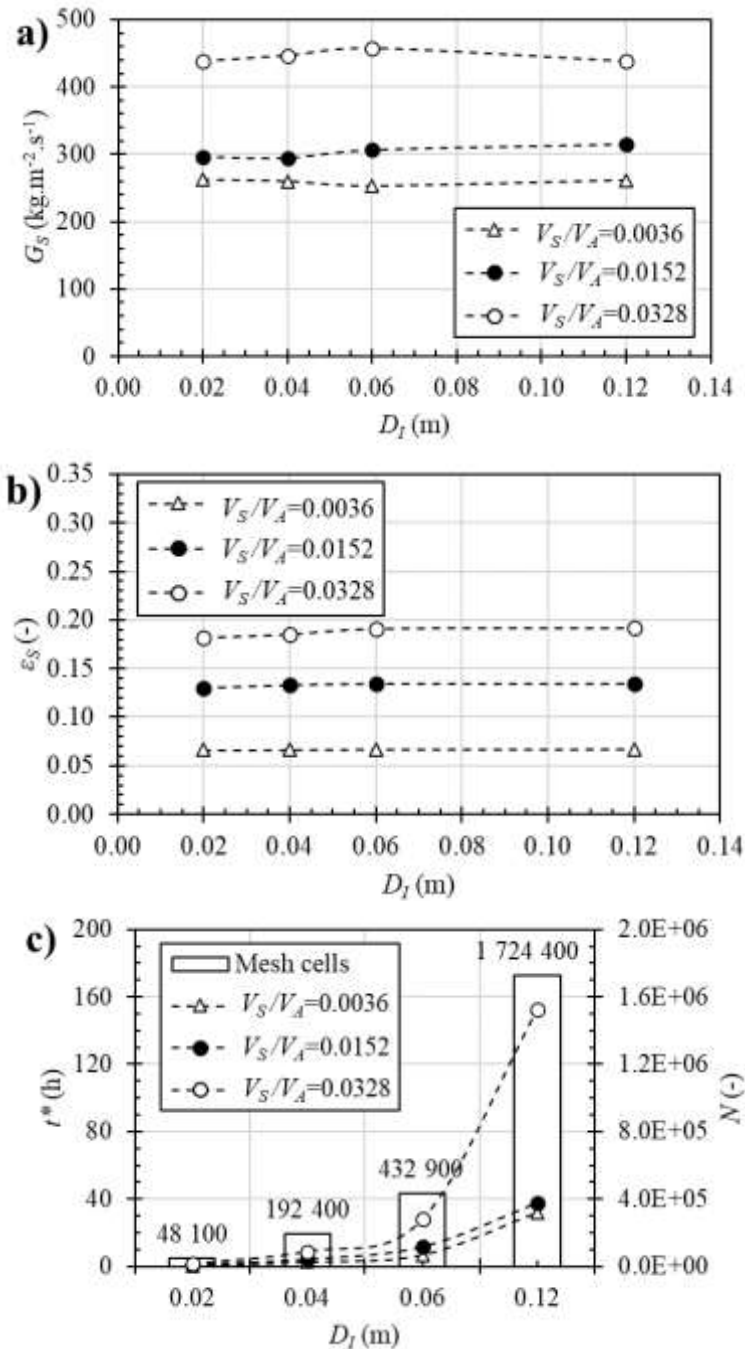
375
 376 **Fig. 9.** Solids mass flux as a function of a) P , b) V_A , and c) V_A^* , as well as d) initial settings for marked points (1)
 377 to (3) with $V_S/V_A=0.015$ and e) solids flow concentration versus V_A .

378 3.6 Model extrapolation: effect of the injector diameter

379 In this section, the numerical model is used to simulate injectors with larger internal
 380 diameters aiming at evaluating feeders for larger scale applications in a cost-effective way.
 381 Three different operating conditions were tested to cover dilute to dense injections, with V_S/V_A
 382 of 0.0036 (test 1), 0.0152 (test 5), and 0.0328 (test 8). The simulation setup and the cell size is
 383 equal to that validated in Section 3.3, however the initial condition for solids and gas were
 384 adjusted to match the same V_S/V_A ratio since the injector volume increases with increasing D .
 385 Thus, the gas pressure in the pressurized chamber was maintained at 500 kPa, equal to tests 1,
 386 5, and 8 (Table 1), whereas the initial mass of solids was increased to meet similar V_S/V_A . It
 387 means that batch injections of sawdust were performed from 0.003 to 0.890 kg.

388 The results for mean solids flux and flow concentration are presented in Fig. 10a and 10b,
 389 respectively, for diameters from 0.02 to 0.12 m, with the latter representing a 6-fold increase of
 390 this parameter. Similar values for G_S and ε_s are observed in the range of $0.02 \leq D_I \leq 0.12$ m, for
 391 all different initial conditions of V_S/V_A . It indicates, at least according to these simulations, that
 392 wall effects are not predominant to jeopardize the performance of this injector for $D_I \geq 0.02$ m,
 393 providing an important conclusion for developing scale-up and operation rules for this solids

394 injector. Ultimately, the operation map shown previously (Fig 9b and 9c) might also be
 395 employed for estimating G_S for injectors with $D_I \geq 0.02$ m.



396

397

398

399 **Fig. 10.** Results for different injector diameters (D), in terms of a) solids mass flux (G_S), b) solids flow
 400 concentration (ϵ_S), and c) simulation time (t^*) and number of cells (N).

401 In Fig. 10c, the simulation time (t^*) and number of cells are presented for different D_I and
 402 V_S/V_A . There is an exponential increase in t^* with increasing D_I because the mesh cells in the
 403 geometry also increases exponentially. The same mesh density of 162 cells/ cm^3 (i.e., same cells
 404 size) has been used in the simulations to prevent mesh-related uncertainties in the calculations.

405 Moreover, for implementation purposes, it is important to highlight that simulations with
406 greater initial quantity of solids (i.e., those with higher V_S/V_A) demand more time to be finished
407 with the Barracuda software because of the higher number of clouds to track. For example, in
408 our case, the simulations with V_S/V_A of 0.0328 takes from 2.5 to 4.8 times more time to finish
409 than those with V_S/V_A of 0.0036.

410 **4 Conclusions**

411 In this study, the applicability of a commercial CFD code with the MP-PIC approach is
412 demonstrated to simulate the transport of biomass with a pressurized gas feeder. After testing
413 against experimental data, the numerical model is used to simulate various operation conditions
414 (P and M), and to study the system transient hydrodynamics. The model is then extrapolated,
415 and an operation map is build-up for the injector as a function of dimensionless parameters
416 related to the initial solids loading and driving force intensity (V_S/V_A and V_A). The model is also
417 extrapolated to study the influence of the injector diameter (D_I) which is a key parameter for
418 injector's scale-up.

419 The experimental results were accurately reproduced after some investigations on the
420 drag law and particle-to-wall parameters. The drag law was more important to tune G_S while
421 the particle-wall interactions affected the accumulation of powders in the injection line (R). The
422 solid-stress tensor function used in Barracuda, Eq. (16), is notably simpler than the set of
423 equations employed by the kinetic theory of granular flow. Thus, careful analysis should be
424 performed to assess the suitability of Eq. (16) to different applications, particularly for dense
425 systems. The nature of the multiphase flow analyzed here, consisting of a dilute batch flow of
426 solids ($\varepsilon_S < 0.20$) may have contributed to some extent to the good model predictions.

427 In terms of the simulation results, the model has been extrapolated to different conditions
 428 of gas pressures and injector diameters in Sections 3.5 and 3.6. An assessment of the deviations
 429 of these predictions should be performed in the future with the availability of experimental data.

430 Future studies could simulate this solids injector with powders of different properties
 431 (particle density and size distribution) to cover other applications. Besides, further
 432 investigations could focus on validating the model for predicting gas-solid jet penetration in
 433 fixed and fluidized beds with this injector.

434 5 Nomenclature

A	Cross-sectional area of the injection line (m^2)
c_0 to c_{15}	Drag function constants (-)
D	Drag function (-)
D_I	Injector diameter (m)
d_p	Particle diameter (m)
d_{10}	Volumetric diameter for 10% of samples' particle-size (μm)
d_{50}	Volumetric diameter for 50% of samples' particle-size (μm)
d_{90}	Volumetric diameter for 90% of samples' particle-size (μm)
F	Gas-solid momentum exchange rate (kPa)
f	Particle probability distribution
f_e	Drag function parameter (-)
\vec{g}	Gravity acceleration ($\text{m}\cdot\text{s}^{-2}$)
G_S	Solids mass flux ($\text{kg}\cdot\text{m}^{-2}\cdot\text{s}^{-1}$)
I	Unit tensor (-)
M	Initial mass of sawdust in the injector (kg)
$M_{99.5\%}$	Mass of sawdust at 99.5% of the cumulative curve in plane III (kg)
M^*	Cumulative mass of sawdust passing through plane III (kg)
M	Maximum momentum redirection from collisions (%)
m_p	Mass of a particle cloud (kg)
N	Number of mesh cells (-)
P	Air pressure in the injector (kPa)
P_{ref}	Reference air pressure (kPa)
P_S	Constant in Eq. (16) (kPa)
p_p^{n+1}	Pressure interpolated to cloud position at instant $n+1$ (kPa)
Q_S	Volumetric solid flowrate (m^3)
Q_t	Volumetric total gas flowrate (m^3)
R	Mass of sawdust accumulated on the injection line (%)
Re	Reynolds number (-)
T	Time (s)
t_e	Experimental injection flow time (s)
t^*	Simulation time (h)
$t_{99.5\%}$	Simulated injection flow time (s)

T_{ref}	Reference air temperature (K)
\vec{u}_g	Gas phase velocity vector ($\text{m}\cdot\text{s}^{-1}$)
$U_{g,p}^{n+1}$	Gas velocity interpolated to cloud position at instant $n+1$ ($\text{m}\cdot\text{s}^{-1}$)
\vec{u}_p	Particle cloud velocity vector ($\text{m}\cdot\text{s}^{-1}$)
\vec{u}_p^n	Particle cloud velocity vector at instant n ($\text{m}\cdot\text{s}^{-1}$)
\vec{u}_p^{n+1}	Particle cloud velocity vector at instant $n+1$ ($\text{m}\cdot\text{s}^{-1}$)
U_p^{n+1}	
\vec{u}_s	Solid phase velocity vector ($\text{m}\cdot\text{s}^{-1}$)
U	Secondary air velocity ($\text{m}\cdot\text{s}^{-1}$)
U_t	Total air velocity ($\text{m}\cdot\text{s}^{-1}$)
U_S	Cross-sectional solids velocity ($\text{m}\cdot\text{s}^{-1}$)
V	Volume of the pressurized chamber (m^3)
V_A	Initial volume of air defined in Eq. (2) (-)
V_A^*	Initial volume of air defined in Eq. (20) (-)
V_S/V_A	Volume of solids divided by volume of air as in Eq. (1) (-)
x_p^n	Cloud position at instant n (m)
x_p^{n+1}	Cloud position at instant $n+1$ (m)

Greek letter

α_g	Gas phase fraction (-)
α_s	Solid phase fraction (-)
$\alpha_{s,max}$	Parameter in Eq. (16) (-)
β	Parameter in Eq. (16) (-)
∇P	Pressure gradient in the system (kPa)
Δt	Simulation time step (s)
η_n	Normal particle-to-wall retention parameter (-)
η_t	Tangent particle-to-wall retention parameter (-)
ε	Mean air fraction in the flow (-)
ε_S	Mean solid fraction in the flow (-)
ε_p	Parameter in Eq. (16) (-)
μ_g	Gas viscosity ($\text{kg}\cdot\text{m}^{-1}\cdot\text{s}^{-1}$)
ω	Drag function parameter (-)
ρ_g	Air density ($\text{kg}\cdot\text{m}^{-3}$)
ρ_m	Mean bulk density ($\text{kg}\cdot\text{m}^{-3}$)
ρ_p	Particle density ($\text{kg}\cdot\text{m}^{-3}$)
ρ_s	Solid phase density ($\text{kg}\cdot\text{m}^{-3}$)
θ	Angle of impact particle-to-wall ($^\circ$)
τ_g	Gas phase stress tensor (kPa)
τ_p^{n+1}	Solid stress interpolated to instant $n+1$ (kPa)
τ_s	Solid phase stress tensor (kPa)

435 **6 References**

- 436 Amblard, B., Bertholin, S., Bobin, C., Gauthier, T., 2015. Development of an attrition
437 evaluation method using a Jet Cup rig. Powder Technology 274, 455–465.
438 10.1016/j.powtec.2015.01.001.

439 Andrews, M.J., O'Rourke, P.J., 1996. The multiphase particle-in-cell (MP-PIC) method for
440 dense particulate flows. *International Journal of Multiphase Flow* 22 (2), 379–402.
441 10.1016/0301-9322(95)00072-0.

442 Ariyaratne, W.H., Ratnayake, C., Melaaen, M.C., 2017. Application of the MP-PIC method
443 for predicting pneumatic conveying characteristics of dilute phase flows. *Powder*
444 *Technology* 310, 318–328. 10.1016/j.powtec.2017.01.048.

445 Bai, Y., Si, H., 2021. Experimental study on feeding characteristics of conical bottom
446 pneumatic spout feeder for biomass pyrolysis. *Chemical Engineering and Processing -*
447 *Process Intensification* 166, 108490. 10.1016/j.cep.2021.108490.

448 Bandara, J.C., Thapa, R., Nielsen, H.K., Moldestad, B.M.E., Eikeland, M.S., 2021.
449 Circulating fluidized bed reactors – part 01: analyzing the effect of particle modelling
450 parameters in computational particle fluid dynamic (CPFD) simulation with experimental
451 validation. *Particulate Science and Technology* 39 (2), 223–236.
452 10.1080/02726351.2019.1697773.

453 Berruti, F.M., Ferrante, L., Berruti, F., Briens, C., 2009. Optimization of an Intermittent Slug
454 Injection System for Sawdust Biomass Pyrolysis. *International Journal of Chemical*
455 *Reactor Engineering* 7 (1). 10.2202/1542-6580.2077.

456 Chen, C., Werther, J., Heinrich, S., Qi, H.-Y., Hartge, E.-U., 2013. CPFD simulation of
457 circulating fluidized bed risers. *Powder Technology* 235, 238–247.
458 10.1016/j.powtec.2012.10.014.

459 Chladek, J., Jayarathna, C.K., Moldestad, B.M., Tokheim, L.-A., 2018. Fluidized bed
460 classification of particles of different size and density. *Chemical Engineering Science* 177,
461 151–162. 10.1016/j.ces.2017.11.042.

462 Dai, J., Cui, H., Grace, J.R., 2012. Biomass feeding for thermochemical reactors. *Progress in*
463 *Energy and Combustion Science* 38 (5), 716–736. 10.1016/j.pecs.2012.04.002.

464 Dai, J., Grace, J.R., 2011. Biomass granular screw feeding: An experimental investigation.
465 *Biomass and Bioenergy* 35 (2), 942–955. 10.1016/j.biombioe.2010.11.026.

466 Dhiman, J., Shrestha, A., Fasina, O., Adhikari, S., Via, B., Gallagher, T., 2016. Physical,
467 ignition, and volatilization properties of biomass feedstocks dusts. *Trans. ASABE* 58,
468 1425–1437.

469 Feng, M., Li, F., Wang, W., Li, J., 2018. Parametric study for MP-PIC simulation of bubbling
470 fluidized beds with Geldart A particles. *Powder Technology* 328, 215–226.
471 10.1016/j.powtec.2018.01.024.

472 Fotovat, F., Abbasi, A., Spiteri, R.J., Lasa, H. de, Chaouki, J., 2015. A CPFD model for a
473 bubbly biomass–sand fluidized bed. *Powder Technology* 275, 39–50.
474 10.1016/j.powtec.2015.01.005.

475 Gidaspow, D., 1994. Kinetic theory approach, in: , *Multiphase Flow and Fluidization*.
476 Elsevier, pp. 239–296.

477 Gomes, T.L., Lourenço, G.A., Ataíde, C.H., Duarte, C.R., 2021. Biomass feeding in a dilute
478 pneumatic conveying system. *Powder Technology* 391, 321–333.
479 10.1016/j.powtec.2021.06.020.

480 Haider, A., Levenspiel, O., 1989. Drag coefficient and terminal velocity of spherical and
481 nonspherical particles. *Powder Technology* 58 (1), 63–70. 10.1016/0032-5910(89)80008-
482 7.

483 Ilic, D., Williams, K., Farnish, R., Webb, E., Liu, G., 2018. On the challenges facing the
484 handling of solid biomass feedstocks. *Biofuels, Bioprod. Bioref.* 12 (2), 187–202.
485 10.1002/bbb.1851.

486 Kraft, S., Kirnbauer, F., Hofbauer, H., 2017. CFPD simulations of an industrial-sized dual
487 fluidized bed steam gasification system of biomass with 8 MW fuel input. *Applied Energy*
488 190, 408–420. 10.1016/j.apenergy.2016.12.113.

489 Kraft, S., Kirnbauer, F., Hofbauer, H., 2018. Influence of drag laws on pressure and bed
490 material recirculation rate in a cold flow model of an 8 MW dual fluidized bed system by
491 means of CFPD. *Particuology* 36, 70–81. 10.1016/j.partic.2017.04.009.

492 Lun, C.K.K., Savage, S.B., Jeffrey, D.J., Chepurniy, N., 1984. Kinetic theories for granular
493 flow: inelastic particles in Couette flow and slightly inelastic particles in a general
494 flowfield. *J. Fluid Mech.* 140, 223–256. 10.1017/S0022112084000586.

495 Massaro Sousa, L., Amblard, B., Montjovet, F., Tebianian, S., 2021. Characterization of a
496 pressurized feeder for biomass injection into gas-solid systems. *Chemical Engineering*
497 *Research and Design* 175, 171–181. 10.1016/j.cherd.2021.08.024.

498 Massaro Sousa, L., Ferreira, M.C., 2019. Spent coffee grounds as a renewable source of
499 energy: an analysis of bulk powder flowability. *Particuology* 43, 92–100.

500 Massaro Sousa, L., Ferreira, M.C., 2020a. Analysis of the performance of an L-valve feeding
501 spent coffee ground powders into a circulating fluidized bed. *Powder Technology* 362,
502 759–769. 10.1016/j.powtec.2019.12.010.

503 Massaro Sousa, L., Ferreira, M.C., 2020b. On the performance of a spouted bed type device
504 for feeding spent coffee grounds to a circulating fluidized bed reactor. *Chemical*
505 *Engineering Research and Design* 160, 31–38. 10.1016/j.cherd.2020.05.002.

506 McKendry, P., 2002. Energy production from biomass (part 1): overview of biomass.
507 *Bioresource Technology* 83 (1), 37–46. 10.1016/S0960-8524(01)00118-3.

508 Pal, K., Theuerkauf, J., 2021. Multiphase Particle in Cell Simulations of Fluidized Beds:
509 Studies on Bubble Rise Velocity and Minimum Fluidization Velocity. *Chemie Ingenieur*
510 *Technik* 93 (1-2), 237–246. 10.1002/cite.202000201.

511 Perea-Moreno, M.-A., Samerón-Manzano, E., Perea-Moreno, A.-J., 2019. Biomass as
512 Renewable Energy: Worldwide Research Trends. *Sustainability* 11 (3), 863.
513 10.3390/su11030863.

514 Ramírez-Gómez, Á., 2016. Research needs on biomass characterization to prevent handling
515 problems and hazards in industry. *Particulate Science and Technology* 34 (4), 432–441.
516 10.1080/02726351.2016.1138262.

517 Snider, D.M., 2001. An Incompressible Three-Dimensional Multiphase Particle-in-Cell
518 Model for Dense Particle Flows. *Journal of Computational Physics* 170 (2), 523–549.
519 10.1006/jcph.2001.6747.

520 Solnordal, C.B., Kenche, V., Hadley, T.D., Feng, Y., Witt, P.J., Lim, K.-S., 2015. Simulation
521 of an internally circulating fluidized bed using a multiphase particle-in-cell method.
522 *Powder Technology* 274, 123–134. 10.1016/j.powtec.2014.12.045.

523 Sung, W.C., Kim, J.Y., Chung, S.W., Lee, D.H., 2021. Effect of particle size distribution on
524 hydrodynamics of pneumatic conveying system based on CFPD simulation. *Advanced*
525 *Powder Technology* 32 (7), 2336–2344. 10.1016/j.appt.2021.05.010.

526 Tannous, K., Lam, P.S., Sokhansanj, S., Grace, J.R., 2013. Physical properties for flow
527 characterization of ground biomass from Douglas fir wood. Part. Sci. Technol. 31, 291–
528 300.

529

530 Tu, Q., Wang, H., 2018. CPFD study of a full-loop three-dimensional pilot-scale circulating
531 fluidized bed based on EMMS drag model. Powder Technology 323, 534–547.
532 10.1016/j.powtec.2017.09.045.

533 Turton, R., Levenspiel, O., 1986. A short note on the drag correlation for spheres. Powder
534 Technology 47 (1), 83–86. 10.1016/0032-5910(86)80012-2.

535 Woodruff, R.B., Kreider, P., Weimer, A.W., 2012. A novel brush feeder for the pneumatic
536 delivery of dispersed small particles at steady feed rates. Powder Technology 229, 45–50.
537 10.1016/j.powtec.2012.06.002.

538 Yang, N., Wang, W., Ge, W., Wang, L., Li, J., 2004. Simulation of Heterogeneous Structure
539 in a Circulating Fluidized-Bed Riser by Combining the Two-Fluid Model with the EMMS
540 Approach. Ind. Eng. Chem. Res. 43 (18), 5548–5561. 10.1021/ie049773c.

541